



Final Draft of the original manuscript

Lage, S.; Campanelli, L.; Guerra, A.; Shen, J.; dos Santos, J.; da Silva, P.; Bolfarini, C.:

A study of the parameters influencing mechanical properties and the fatigue performance of refill friction stir spot welded AlMgSc alloy.

In: The International Journal of Advanced Manufacturing Technology. Vol. 100 (2019) 101 – 110.

First published online by Springer: 22.09.2018

<https://dx.doi.org/10.1007/s00170-018-2696-0>

A study of the parameters influencing mechanical properties and the fatigue performance of refill friction stir spot welded AlMgSc alloy

Sara Beatriz Miranda Lage¹ & Leonardo Contri Campanelli¹ & Ana Paula de Bribean Guerra¹ & Junjun Shen² & Jorge Fernandez dos Santos² & Paulo Sergio Carvalho Pereira da Silva¹ & Claudemiro Bolfarini¹

Abstract

Friction spot welds of 1.6-mm-thick AlMgSc alloy were investigated in this work. A design of experiment method was used to evaluate the effect of process parameters on the shear static strength. The optimized condition of parameters was employed in the assessment of the fatigue behavior. The typical hook feature was minimized by restricting the tool penetration into only the upper sheet. As a consequence, shear strength was sensitive to the extension of the welded region rather than the hook morphology. The fatigue performance was affected by the multiple crack initiation sites that resulted from a complex stress state during the axial loading. Striations were observed in practically the entire crack propagation region, suggesting that unstable fatigue crack growth did not take place in this specific weld configuration.

1 Introduction

AlMgSc alloy is currently being considered for automotive and aerospace applications due to the lower density, similar yield strength, and higher fracture toughness than the aerospace AA2024 alloy [1] and due to the lower cost than the Li-containing Al-alloys [2]. Nano-sized, coherent Al₃Sc precipitates are responsible for the hardening of the Al-matrix, in addition to the solid solution effect of Mg [3]. Contrary to the hardening precipitates responsible for the mechanical property enhancement of 2XXX and 7XXX alloys, these precipitates are stable at high temperatures, presenting no significant growth until 400 °C, which renders the AlMgSc alloys higher mechanical properties than the ones of 2XXX and 7XXX series at high temperatures. In addition, this stability has an important

metallurgical effect pinning grain growth and keeping a fine grain sized microstructure, which benefit the mechanical properties significantly [3]. Dos Santos et al. [4] studied the behavior of the Al₃Sc precipitates by friction stir welding (FSW) in butt joint configuration. Transmission electron microscopy analysis showed the presence of the precipitates in the base metal as well as in the welded zone, with no increase in the size or any significant dissolution. Zhao et al. [5] compared the microstructure and the mechanical properties of AlMgSc butt joints produced by FSW and tungsten inert gas (TIG). The softening effect of precipitate dissolution was considerably lower by FSW, which led to higher efficiency of the FSW joint: 19% higher tensile strength than the TIG joint and 94% tensile strength of the base metal. Noteworthy is that AlMgSc welds have been studied in butt configuration so far.

Refill friction stir spot welding (refill FSSW) or friction spot welding (FSpW) is a solid-state joining process that allows joining two or more sheets in overlap configuration [6]. This process allows production of welds without solidification defects, keyhole surface, or increasing of weight. Thus, refill FSSW has been successfully applied in joining similar and dissimilar metals. More recently, the joining of AA2198 aluminum alloy has been reported by de Barros et al. [7]. Santana et al. [8] have evaluated the welding of the novel ultra-high-strength AlMgSi alloy. These works and several others on

Table 1 Mechanical properties of the KO8542 alloy used in this work

YS (MPa)	UTS (MPa)	ϵ (%)	Microhardness (HV)
330 ± 1	411 ± 2	7.13 ± 0.75	113 ± 2

refill FSSW of similar metal sheets have shown the presence of a weld feature, named hook, in various welding conditions. Badarinarayan et al. [9] defined hook as a geometrical feature due to the upward bending of the interface between both sheets during the sleeve penetration. Rosendo et al. [10] showed that the hook geometry significantly influenced the fracture mode of AA6181-T4 welds and caused the decrease in lap shear strength. Furthermore, hook was a preferential region where fatigue crack may initiate and propagate. The presence of hook in AZ31 magnesium alloy welds was also verified by Campanelli et al. [11], who concluded that lap shear strength is optimized when the vertical displacement of hook region is minimized.

With small sized hooks, the extension of the welded region plays a significant role in the mechanical performance. Santana et al. [8] suggested a threshold value for the hook height, below which the bonded width has the main influence on the weld strength. A combined effect of hook height and bonded width was also reported by Cao et al. [12] in AA6061-T6 welds. Concerning the fatigue behavior of friction spot welds, Effertz et al. [13] studied the fatigue properties of similar AA7050-T76 aluminum joints, while Plaine et al. [14] evaluated the behavior of dissimilar AA5754/Ti6Al4V joints. In both works, fatigue lives above 10^6 cycles were only obtained at considerably low stress levels. The former reported a fatigue limit of 10% of the static shear strength, while the latter obtained 15% of the static shear strength. These works are, however, lacking of a better explanation of the fatigue crack

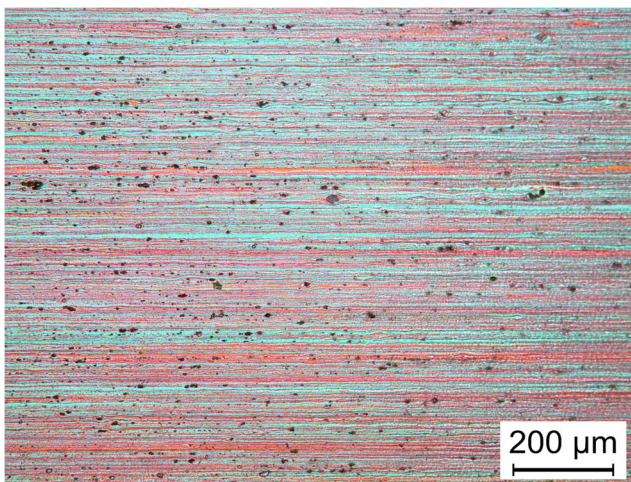


Fig. 1 Microstructure of the base metal. The black points are FeMn particles

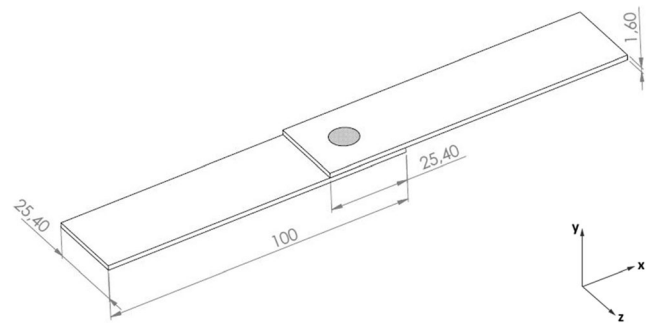


Fig. 2 Illustration of the welded samples

evolution and are more restricted to delivering fatigue data of the joints.

Given the importance of the spot welding for manufacturing, the objective of this study was to obtain a satisfactory static shear performance of friction spot joints of the newly developed low density and high strength AlMgSc alloy, through a study of welding parameter optimization. Moreover, the evaluation of the fatigue behavior was also intended. Fatigue crack nucleation and propagation were investigated in order to allow a better understanding of the crack development in this complex welding configuration.

2 Experimental procedure

The material used in this study was the KO8542 alloy, which is a AlMgSc alloy. The average yield strength (YS), ultimate tensile strength (UTS), elongation at fracture (A), and microhardness at room temperature are presented in Table 1. The microstructure of the base metal, shown in Fig. 1, is composed of a pancake-shaped grain structure, that is, elongated, not recrystallized, and deformed grains aligned with the rolling direction. FeMn constituent particles are distributed in the matrix (dark points in Fig. 1). The samples consisted of 1.6 mm thick, 100 mm length, and 25.4 mm width sheets, welded in an overlap configuration with 25.4 mm overlap according to the AWS D17.2/D17.2M specification [15], as illustrated in Fig. 2.

The welds were performed in a RPS 100 machine through the sleeve plunge variant [10]. The tool consisted of three independent components: a clamping ring, a threaded sleeve, and a threaded pin, with diameters of 14.5, 9, and 6 mm, respectively. Rosendo et al. [10] illustrate the tool shape of RSSW process. The three process parameters varied in this

Table 2 Material properties used in FEA [16]

Material	E (GPa)	Poisson's ratio
AlMgSc	74	0.33



Fig. 3 Cross-section macrograph (yz-plane) showing the different zones. The arrows indicate the hook region in the SZ-TMAZ boundary

study were plunge time (0.75–1.5 s), rotational speed (1000–2000 rpm), and plunge depth (1.2–1.6 mm). Clamping force was maintained at 9.25 kN and dwell time was 0 s. In the design of experiments, an L9 orthogonal array was designed by Taguchi method, meaning that nine combinations of parameters were generated. The results were evaluated in terms of means and signal-to-noise (S/N) ratio, which, respectively, refers to the average value of the static shear load and the deviation of the quality characteristic from the optimum value. In order to maximize the response, “the-higher-the-better” criterion was employed in the optimization process.

Static lap shear tests were carried out at room temperature using a screw-driven Zwick-Roell 1478 testing machine and a constant cross-head speed of 1 mm/min, with three replicates for each welding condition. The best condition of parameters obtained from the design of experiments in terms of static shear strength was subjected to fatigue tests. The tension-tension fatigue tests ($R=0.1$) were performed at room temperature and a frequency of 10 Hz using a servo-hydraulic Schenck Instron testing machine in load control mode. If specimen failure was not reached, the test was interrupted at 2×10^6 cycles. Three specimens were tested at each of the five stress levels, which were determined as fractions of the static shear strength. Similarly to Effertz et al. [13], Weibull distribution was used to analyze statistically the fatigue life and to obtain a S-N curve.

Microstructural characterization was performed in a Leica DMI4000 M optical microscope after polishing with colloidal silica and electrolytic etching with Barker’s reagent. Due to the microstructural refinement, grain size measurements were conducted in an FEI Quanta 650 FEG scanning electron

microscope (SEM). The same equipment was used in the observation of the fracture surfaces after the fatigue tests.

For an estimation of the stress distribution acting nearby the hook and to analyze the fracture initiation mode, finite element analysis (FEA) was performed using Simulation software, which is a tool integrated with SolidWorks CAD software, version 2015 SP4.0. A linear static analysis was conducted using Large Problem Direct Sparse solver type due to large deformation during the test, which is the most appropriate algorithm to model the behavior of the material under large deformation. The 3D model was constructed as an assembly constituted of three parts, two equal parts modeling the aluminum plates with a hole, where the weld was inserted as a different part in order to be able to define a small region with a crack, which was defined as a no-penetration contact type rather than bonded, as the welded regions. With the same material properties of the plates, the weld was represented as a cylinder with two division lines in the longitudinal face, forming a separated surface of 50 μm in extension, to represent a discontinuity in the weld neighborhood. The mesh contact type between this surface and one of the plates was configured with a no-penetration contact mesh, being present in only one of the plates. The mesh of the rest of contact surfaces between the weld and plates was configured as bonded. The components were modeled with a linear elastic material using the material properties presented in Table 2.

The mesh was built with tetrahedral elements by meshing scheme Voronoi-Delaunay, which is the default mesh generation scheme used by software for volume meshes, containing a total number of elements of 1.096.819. A mesh refinement was performed on regions of stress concentrators with an element size of 0.05 mm in order to improve result accuracy in this specific region. The mesh interface between both plates was defined as a no-penetration interaction type to describe the non-welded regions only in contact, using a friction coefficient of 0.05 between them. Two different analyses were performed, with differences between the degrees of freedom of the model being tested. In the first analysis, a

Fig. 4 Microstructure of a SZ and b TMAZ

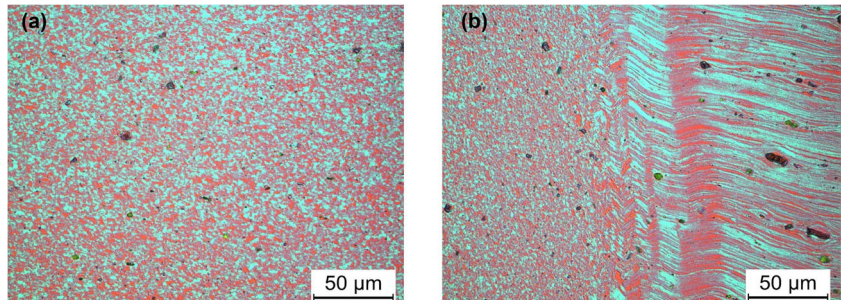


Table 3 L9 orthogonal array and shear load results

Condition	Plunge time (s)	Rotational speed (rpm)	Plunge depth (mm)	Shear load (kN)
1	0.75	1000	1.2	8.64 ± 0.39
2	0.75	1500	1.4	8.48 ± 0.27
3	0.75	2000	1.6	7.96 ± 0.12
4	1	1000	1.4	9.34 ± 0.23
5	1	1500	1.6	9.28 ± 0.31
6	1	2000	1.2	7.30 ± 0.52
7	1.5	1000	1.6	9.18 ± 0.16
8	1.5	1500	1.2	7.89 ± 0.28
9	1.5	2000	1.4	7.86 ± 0.24

region of 25.4 mm (in length) in one plate was fixed to represent the stationary machine clamp. An equal size region was configured in the opposite plate, where a force of 2335 N was applied, resulting in shearing forces on the weld simulating a uniaxial tensile test. In this case, the normal translation related to the faces of the plates was set to be null, avoiding bending stresses due to the elastic deformation of the plates.

3 Results and discussions

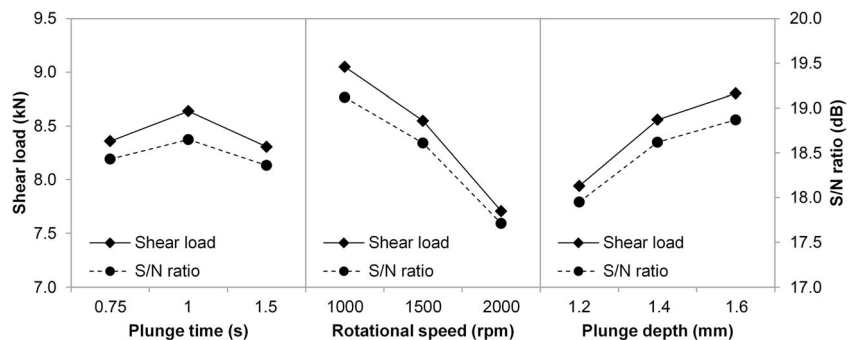
3.1 Microstructure and process optimization

Figure 3 presents a typical cross-section macrograph of the welded joint. The weld has an elliptical shape, and no defects or thickness reduction was observed. As indicated by an arrow, the hook feature is located in the boundary of the welded and non-welded regions. In comparison to the grain structure of the base metal, the following zones can be distinguished: stir zone (SZ), thermo-mechanically affected zone (TMAZ) and heat-affected zone (HAZ). As shown in Fig. 4a, SZ has a dynamic recrystallized structure composed of fine grains due to the high strain rate and temperature in this area, with grain size varying between 0.86 μm and 1.4 μm. Grain coarsening

is inhibited by the pre-existing and thermally stable Al₃Sc precipitates, which are not dissolved or changed during the welding process because of the short thermal cycle [17]. TMAZ shown in Fig. 4b is subjected to a lower degree of heat and deformation, so that only partial recrystallization occurs. In part of this region, the pancake-shaped grains of the base metal are simply rotated to the upwards direction by the tool motion. HAZ preserves the microstructural appearance of the base metal, possibly due to the thermal stability of the alloy regarding grain growth, since the presence of Sc-containing precipitates prevents recrystallization processes, as similarly reported on FSW by Zhao et al. [5].

The L9 orthogonal array with the experimental values of shear load is shown in Table 3. The shear load varied between 7.30 ± 0.52 kN (condition 6) and 9.34 ± 0.23 kN (condition 4) in the processing window under investigation. The AWS D17.2/D17.2M specification [15] states that the minimum failure load value for 1.6 mm thick aluminum alloy having an ultimate tensile strength above 386 MPa is 3.64 kN. This means that all welds obtained in the present work had a shear load value adequate for aerospace application. The main effect plots for the shear load means and signal-to-noise ratios are presented in Fig. 5. The flatness profile of the plunge time curves indicates a low effect of this parameter on the shear load, with the intermediate level providing a slightly better

Fig. 5 Main effects plots for mean shear load and S/N ratio



weld quality. Rotational speed plots suggest a decrease of this parameter to obtain improved shear load values, while plunge depth plots follow the opposite trend.

By adopting “the-higher-the-better” as the optimization criterion in the design of experiments, the best settings to optimize the shear load are suggested to comprise 1 s, 1000 rpm, and 1.6 mm, respectively, of plunge time, rotational speed, and plunge depth. As long as this combination of parameters is not in the Taguchi design, welds were performed (hereinafter entitled condition 10) and subjected to mechanical testing, resulting in a shear load value of 8.89 ± 0.23 kN. This value is lower than the ones obtained with three conditions of the L9 orthogonal array (4, 5, and 7), probably indicating that the interactions of parameters, which are not considered by the Taguchi design, may have an influence on the shear load. Figure 6 summarizes the shear load results obtained in all welding conditions. The dotted lines comprise the variation range determined by the best mean shear load. The overlapping of the standard deviation bars denotes that there are no significant statistical differences in the shear load values of at least three conditions (4, 5, and 7), with other two conditions (1 and 10) very close the variation range of the best condition of the L9 orthogonal array.

The hook feature and the extension of the welded region are known to affect the mechanical performance of similar friction spot joints [8]. Since the hook height, and therefore the capacity of acting as a stress concentrator, is typically larger when the tool penetration is deeper [7], the variation of the plunge depth in the present work was chosen so as to avoid the tool penetration into the bottom sheet (maximum plunge depth of 1.6 mm is equal the sheet thickness). In fact, as illustrated in Fig. 7, the hook size is below $50 \mu\text{m}$ in height

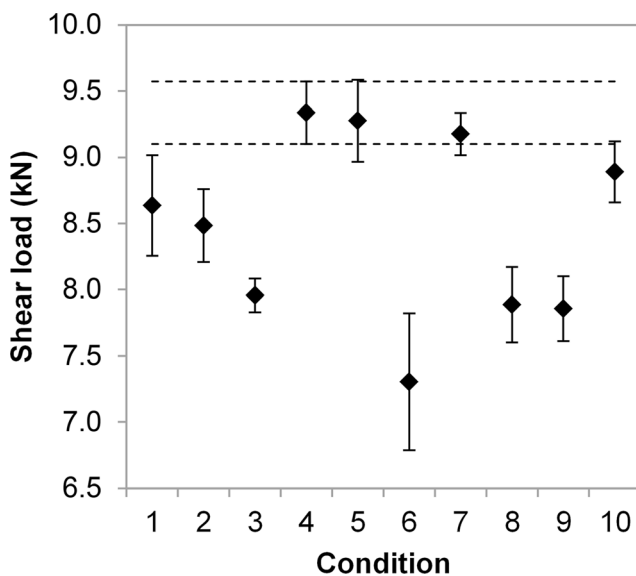


Fig. 6 Mean and standard deviation plots for shear load

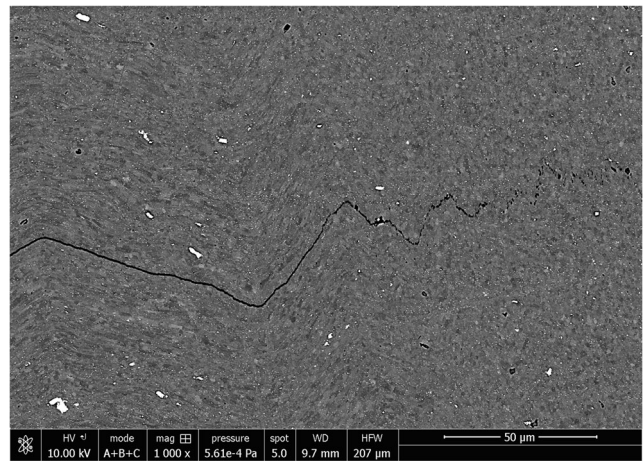


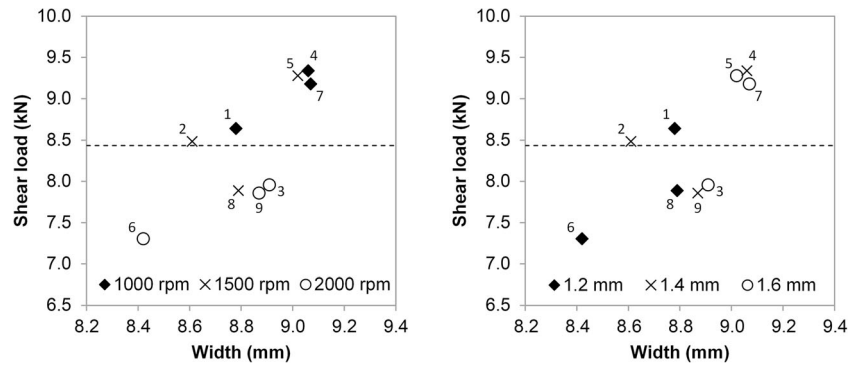
Fig. 7 Micrograph of the hook feature

in all welding conditions, providing a maximum h/t ratio (hook height divided by sheet thickness) of around 3%. This is a very small value when compared, for example, with the values reported by de Barros et al. [7] for equal thick AA2198 friction spot welds, in which the best condition of welding parameters in terms of shear load led to h/t ratio of 13.2%. Therefore, the tool penetration only in the upper sheet could reduce the hook height and, in the processing window under investigation, this factor may not be the main reason for the differences in the shear load results.

Concerning the extension of the welded region, the plot of Fig. 8 reveals that there is a trend of increasing the shear load with the increase of the bonded width. The dotted line comprises the overall average of the shear load results. Since the contribution of the hook feature is low, it is fairly expected that an increased mechanical performance is related to the size of the welded area that comes from the combination of welding parameters. Noteworthy is that all joints produced with 2000 rpm of rotational speed are in the field of shear load values lower than the overall average (below the dotted lines in Fig. 8), but these joints are not necessarily the ones with the smaller bonded width. For the joints produced with 1000 rpm of rotational speed, which is the best level according to the main effect plot (Fig. 5), larger bonded width and shear load value were obtained at the high levels of plunge depth. With total penetration of the tool into the upper sheet, Tier et al. [18] proposed that the reduction of rotational speed creates a more vertical material flow, i.e., towards the weld surface, leading to a smaller bonded width. As this was not the case in our results, it seems that the interaction between the most significant parameters rotational speed and plunge depth plays an important role on determining the extension of the welded region and hence the mechanical performance of the welded joints.

In summary, the condition 4 of the L9 orthogonal array (1 s, 1000 rpm, and 1.4 mm, respectively, of plunge time, rotational

Fig. 8 Correlation of bonded width with shear load (the numbers are the welding conditions). On the left, the data is distinguished by the rotational speed levels and, on the right, by the plunge depth levels



speed, and plunge depth) is considered the optimized one for the improved results, albeit only slightly, of bonded width and shear load. Considering that the average load of 9.34 kN is applied in a nominal area of 63.6 mm² (the area for the tool sleeve diameter), the mean shear stress corresponds to approximately 147 MPa. The calculation of the shear strength based on the tool diameter has been commonly reported in the literature of spot-like welding processes, such as in the works of Cao et al. [12] in AA6061 welds and of Effertz et al. [13] in AA7050 welds. This value of shear strength is used in the following section to build-up the S-N curve.

3.2 Fatigue and fracture behavior

The welds for the fatigue tests were produced with the parameters of condition 4. The stress levels were determined as fractions of the average shear load of 9.34 kN, as detailed in Table 4 along with the fatigue test results. The S-N curve of the experimental data is shown in Fig. 9, in which the power function calculated using the Weibull distribution and the resulting regression curve are also presented. The correlation coefficient $R^2 = 0.97$ of this equation indicates that the regression is an adequate fit to the Weibull data and therefore suitable for a reliable prediction of the fatigue life. From the experimental data, the fatigue limit at 10^6 cycles lies between 5.0 MPa and 6.6 MPa in terms of stress amplitude, being

estimated as 5.8 MPa by the power function. For this stress amplitude value, the maximum stress value is 12.9 MPa and represents approximately 9% of the static shear strength. As discussed by Effertz et al. [13], who obtained a fatigue limit of 10% of the shear strength in AA7050 welds, the joint seems unsafe for high load cyclic solicitations, even with the static shear loads fulfilling the requirements of the AWS D17.2/D17.2M specification [15].

Figure 10 illustrates the two fracture modes obtained after the fatigue tests, namely: through the upper sheet cross section (U) and through the bottom sheet cross section (B). U fracture mode was observed for all stress levels, while B fracture mode particularly occurred under the lower stress level (5.0 MPa) in two out of three specimens tested. For better comprehension, Fig. 11 shows the cross-section macrograph of a fatigue specimen tested at high stress amplitude, but with the test interrupted before the complete fracture. Two cracks can be identified: one propagating towards the upper sheet surface and one propagating towards the bottom sheet surface. This behavior is in agreement with the FEA presented in Fig. 12, because the cracks were initiated in the tensile stress regions around the joint. These stresses are concentrated in the hook, irrespective of its size, and, since this feature is a boundary between the welded and the non-welded regions, the tensile stress field occurs in the entire weld periphery.

Table 4 Levels and results of the fatigue tests

% of shear load	Shear load (kN)		S (MPa)		N _f (cycles to failure)		
	Max.	Amp.	Max.	Amp.	Sample 1	Sample 2	Sample 3
25	2.34	1.05	36.7	16.5	19,943	22,757	26,071
20	1.87	0.84	29.4	13.2	33,997	34,548	36,533
15	1.40	0.63	22.0	9.9	71,575	103,140	129,610
10	0.93	0.42	14.7	6.6	737,152	659,242	664,582
7.5	0.70	0.32	11.0	5.0	> 2,000,000 (no failure in this level)		

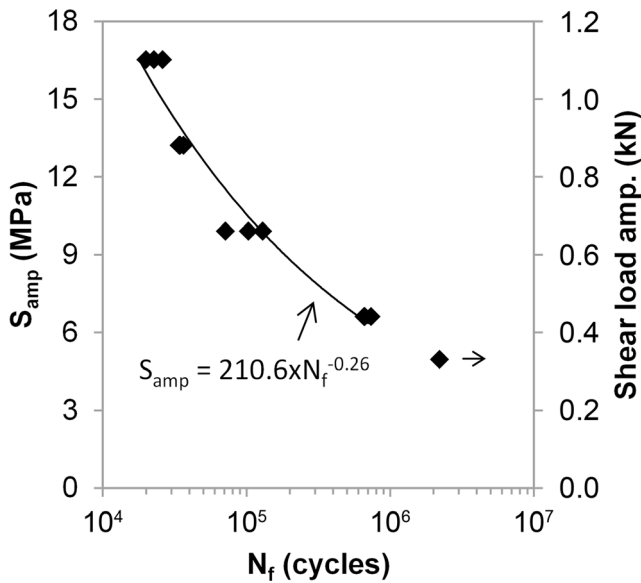


Fig. 9 Fatigue data and S-N curve. The left axis has the stress values, while the right axis has the corresponding load values

In addition, an out-of-plane bending occurs in the system during the axial loading due to the joint geometry and contributes to the opening of the hook in the tensile region. Adib et al. [19] attributed the bending stresses to the typical eccentricity of the spot-like joints and verified that the stress distribution is in fact a combination of the axial and bending components. This study also emphasizes that the gap between thin sheets has a significant influence on the bending moment, resulting in higher tensile stresses and larger plastic zones, as well as reducing the fatigue performance. From the observations in the present work, the hypothesis is that the bending plays an important role by continuously changing the stress state during crack growth, as demonstrated in the sequence with the fracture evaluation. These findings show that one needs to be careful when assessing the literature that deals with the stress distribution around spot welds, because boundary conditions

Fig. 10 Failure modes after the fatigue tests: a through the upper sheet cross section and b through the bottom sheet cross section

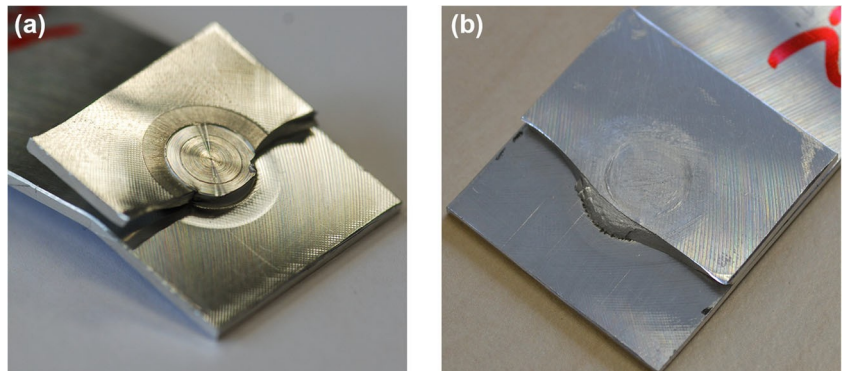


Fig. 11 Cross-section macrograph (xy-plane) of a fatigue tested specimen before fracture. The arrows indicate the loading direction

are typically treated as constant, which is not true under the presence of a fatigue crack.

In spite of the crack propagation towards the upper or bottom surface, the metallurgical aspects observed in the fracture surfaces are similar. Figure 13 presents the macrograph of a typical fracture surface and the SEM micrographs taken in the identified regions. The steps near the interface shown in Fig. 13a reveal multiple initiation sites that occur due to the tensile stresses along the weld periphery. Crack propagation region is characterized by not markedly visible striations (characteristic of brittle striations), as noticed in Fig. 13b. The position of the striations confirms the propagation towards the sheet's outer surface (y-direction), perpendicularly to the loading direction, in the entire weld periphery.

The region of Fig. 13c is no longer in the weld spot, but approximately in the transition of the welded and non-welded regions. The striation pattern is maintained and indicates that the crack propagation also proceeds from the interface to the upper sheet's outer surface. This behavior can be confirmed in Fig. 14 by the orientation of the "beach markings" in the region highlighted by an arrow. Finally, the non-welded region also exhibits striations, as shown in Fig. 13d. The propagation in this region has components in y- and z-directions, but goes back to only y-direction in the area of Fig. 13e, suggesting that another crack nucleated in the interface nearby this region and propagated towards the sheet's outer surface. Figure 13f shows that the striation pattern changes to shear lips only close to the corner of the sheet.

All these observations demonstrate that several crack initiation sites occur in the fatigue test due to the complex stress

Fig. 12 Distribution of the main stress around the weld (xy-plane)

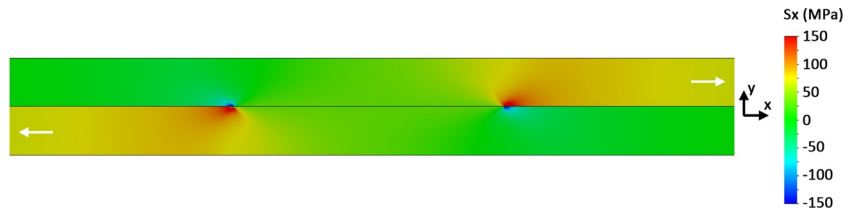
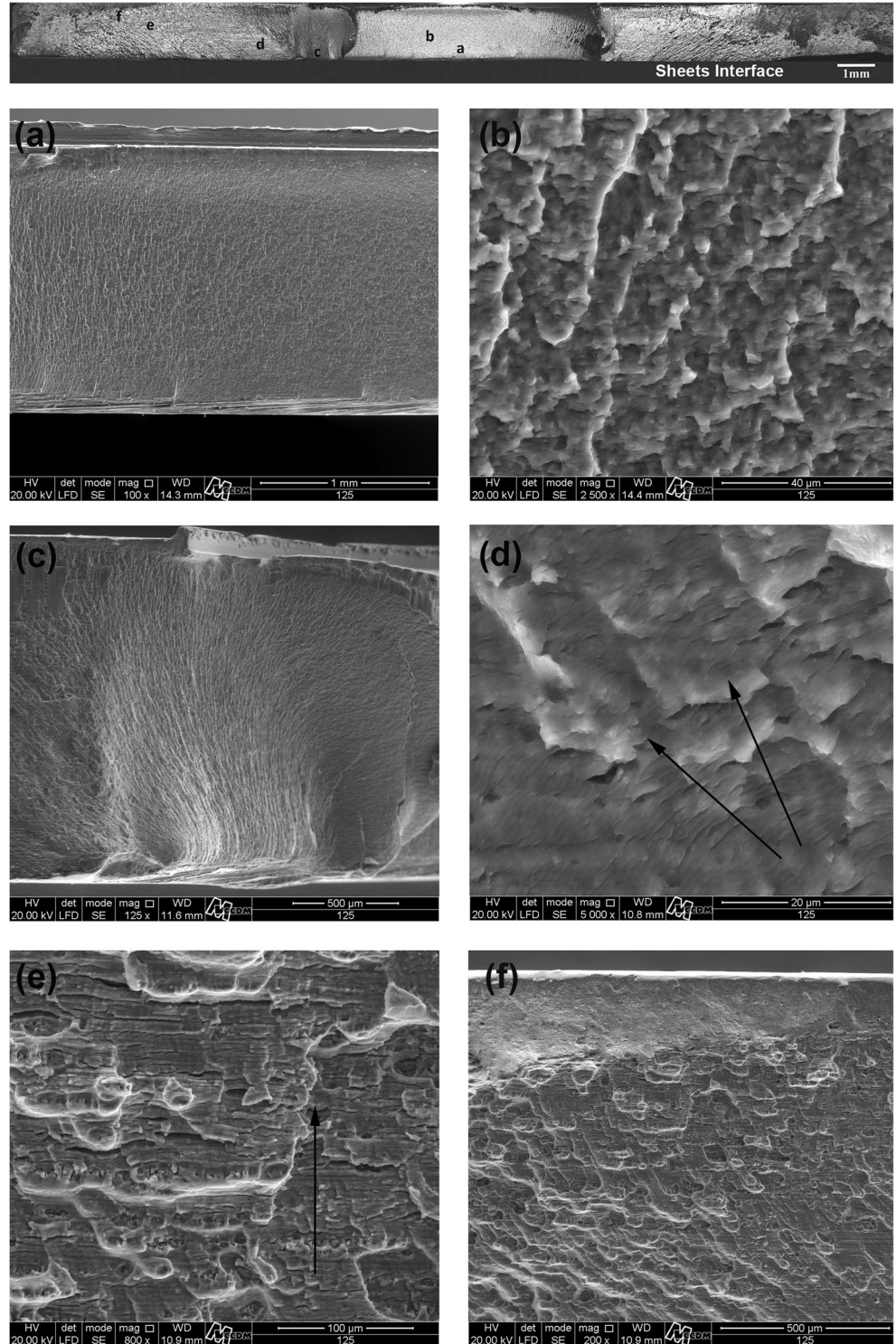


Fig. 13 Macrograph of a typical fracture surface (xz-plane) of the upper sheet and SEM micrographs of the different regions: a steps at the sheets interface; b fatigue striations in the welded region; c transition of the welded and non-welded regions; d, e fatigue striations in the non-welded region; f transition to the shear lip region



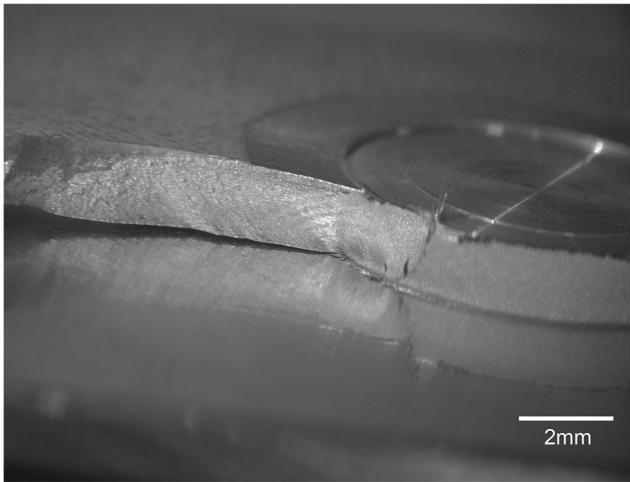


Fig. 14 Orientation of beach markings

state aforementioned, which supports the low fatigue limit usually observed for refill friction stir spot welds (9% of the static shear strength in the present work). The propagation of these cracks developed striations in the whole surface, indicating that the mechanism of crack growth was the same irrespective of the microstructural zone. This also means that the propagation never became unstable for the stress state prevailing in such joints, an indication of the high fracture toughness of this AlMgSc alloy, which is higher than the one for AA2024-T351 alloy [1].

4 Conclusions

The present work assessed the joining of an AlMgSc alloy in overlap configuration by refill friction stir spot welding and the resulting static and fatigue mechanical behaviors. The following conclusions could therefore be drawn:

- (1) The optimum combination of parameters within the studied range and levels was found to be 1 s of plunge time, 1000 rpm of rotational speed, and 1.4 mm of plunge depth, although other combinations showed similar static shear load values.
- (2) Since the penetration of the welding tool was restricted to the upper sheet, the height of the hook feature was not found to be significant to affect the static shear strength. Nevertheless, a trend of increasing the shear strength with the increase of the extension of the welded region was observed.
- (3) The fatigue failure criterion was fulfilled for a maximum stress value of approximately 9% of the static shear strength. Multiple crack nucleation sites, which resulted from the complex stress state generated by the axial and

bending components during the axial loading, accounted for the low fatigue performance.

- (4) The mechanism of fatigue crack growth was based on striations in almost all the fracture surface. Therefore, the propagation through the entire welded and non-welded regions was not unstable, indicating the high fracture toughness of the alloy.

Acknowledgements Authors acknowledge Mr. Manfred Horstmann and Mr. Hamdi Tek for their technical support in performing the fatigue tests.

Funding information This study was financially supported by the Brazilian institutions CNPq and FAPESP (process n. 2016/12995-5).

References

1. Aleris (2015) Aerospace Aluminum AA5028 AlMgSc – The Strong Lightweight. https://www.aleris.com/wp-content/uploads/2016/02/AL-2342_012-Aktualisierung-BR-AlMgSc-2015-06-03-WEB.pdf. Accessed 15 May 2018
2. Pacchione M, Telgkamp J (2006) Challenges of the metallic fuselage. In: 25th International Congress of the Aeronautical Sciences (ICAS 2006)
3. Kendig KL, Miracle DB (2002) Strengthening mechanisms of an Al-mg-Sc-Zr alloy. *Acta Mater* 50(16):4165–4175
4. dos Santos JF, Olea CAW, Coelho RS, Kostka A, Paglia CS, Ghidini T, Donne Eads CD (2010) Metallurgy and weld performance in friction stir welding. In: Lohwasser D, Chen Z (eds) *Friction stir welding – from basics to applications*. Woodhead Publishing, Cambridge, pp 314–410
5. Zhao J, Jiang F, Jian H, Wen K, Jiang L, Chen X (2010) Comparative investigation of tungsten inert gas and friction stir welding characteristics of Al-mg-Sc alloy plates. *Mater Design* 31:306–311
6. Schilling C, dos Santos J (2004) Method and device for linking at least two adjoining work pieces by friction welding. US patent 6,722,556 B2
7. de Barros PAF, Campanelli LC, Alcântara NG, dos Santos JF (2017) An investigation on friction spot welding of AA2198-T8 thin sheets. *Fat Fract Eng Mater Struc* 40:535–542
8. Sanatana LM, Suhuddin UFH, Ölscher MH, Strohaecker TR, dos Santos JF (2017) Process optimization and microstructure analysis in refill friction stir spot welding of 3-mm-thick Al-mg-Si aluminium alloy. *Int J Adv Manuf Tech* 91:1–8
9. Badarinarayan H, Shi Y, Li X, Okamoto K (2009) Effect of tool geometry on hook formation and static strength of friction stir spot welded aluminum 5754-O sheets. *Int J Mach Tools Manuf* 49:814–823
10. Rosendo T, Parra B, Tier MAD, da Silva AAM, dos Santos JF, Strohaecker TR, Alcântara NG (2011) Mechanical and microstructural investigation of friction spot welded AA6181-T4 aluminium alloy. *Mater Design* 32:1094–1100
11. Campanelli LC, Suhuddin UFH, Antonialli AÍS, dos Santos JF, Alcântara NG, Bolfarini C (2013) Metallurgy and mechanical performance of AZ31 magnesium alloy friction spot welds. *J Mater Process Tech* 213:515–521

12. Cao JY, Wang M, Kong L, Guo LJ (2016) Hook formation and mechanical properties of friction spot welding in alloy 6061-T6. *J Mater Process Tech* 230:254–262
13. Effertz PS, Infante V, Quintino L, Suhuddin U, Hanke S, dos Santos JF (2016) Fatigue life assessment of friction spot welded 7050-T76 aluminium alloy using Weibull distribution. *Int J Fatigue* 87:381–390
14. Plaine AH, Suhuddin UFH, Alcântara NG, dos Santos JF (2016) Fatigue behavior of friction spot welds in lap shear specimens of AA5754 and Ti6Al4V alloys. *Int J Fatigue* 91:149–157
15. American Welding Society (2013) Specification for Resistance Welding for Aerospace Applications AWS D17.2/D17.2M, 2nd edn. American Welding Society, Doral
16. Matweb. <http://www.matweb.com/search/DataSheet.aspx?MatGUID=c1de7c6e8a9d45efa06da745e07094a2&ckck=1>. Accessed 5 April 2018
17. Sauvage X, Dédé A, Cabello Muñoz A, Huneau B (2008) Precipitate stability and recrystallisation in the weld nuggets of friction stir welded Al-mg-Si and Al-mg-Sc alloys. *Mater Sci Eng A* 491:364–371
18. Tier MD, Rosendo TS, dos Santos JF, Huber N, Mazzaferro JA, Mazzaferro CP, Strohaecker TR (2013) The influence of refill FSSW parameters on the microstructure and shear strength of 5042 aluminium welds. *J Mater Process Tech* 213:997–1005
19. Adib H, Jeong J, Pluvinage G (2004) Three-dimensional finite element analysis of tensile-shear spot-welded joints in tensile and compressive loading conditions. *Strength Mater* 36:353–364